Constraints from exhumed rocks on the seismic signature of the deep subduction interface

C. M. Tewksbury-Christle[1], W. M. Behr[1]

[1]Structural Geology and Tectonics Group, Geological Institute, Department of Earth Sciences, ETH Zurich, Sonneggstrasse 5, 8092 Zurich, Switzerland

Key Points:

- Seismic velocities of a 3 km fossil subduction interface shear zone are comparable to Low Velocity Zones (LVZs) in modern subduction zones.
- Accounting for fracture and mineral anisotropy in a sediment-dominated interface shear zone results in highly anomalous seismic velocities.
- The LVZ represents the seismic signature of a distributed interface shear zone composed of mixed lithologies.

Corresponding author: Carolyn Tewksbury-Christle, carolyn.tewksbury-christle@erdw.ethz.ch

Abstract

Low Velocity Zones (LVZs) with anomalously high V_p-V_s ratios occur along the downdip extents of subduction megathrusts in most modern subduction zones and are collocated with complex seismic and transient deformation patterns. LVZs are attributed to high pore fluid pressures, but the spatial correlation between the LVZ and the subduction interface, as well as the rock types that define them, remain unclear. We characterize the seismic signature of a fossil subduction interface shear zone in northern California that is sourced from the same depth range as modern LVZs. Deformation was distributed across 3 km of dominantly metasedimentary rocks, with periodic strain localization to km-scale ultramafic lenses. We estimate seismic velocities accounting for mineral and fracture anisotropy, constrained by microstructural observations and field measurements, resulting in a V_p/V_s of 2.0. Comparable thicknesses and velocities suggest that LVZs represent, at least in part, the subduction interface shear zone.

Plain Language Summary

Many subduction zones - places where one tectonic plate goes under another - have areas where seismic waves travel up to three times slower than normal and where the ratio of speeds of two different types of seismic waves is anomalously high. Some researchers have concluded that these Low Velocity Zones (LVZs) at 25-50 km below the surface of the Earth are the undeformed top of a downgoing tectonic plate whereas others suggest that LVZs are zones of intense deformation that allow two tectonic plates to slide past each other. To help resolve this uncertainty, we investigated rocks in a fossil subduction zone that record a history of being subducted and then returned to the surface. We identified the thickness of a zone of deformation and estimated how fast seismic waves would have passed through this zone based on the rock types, how the minerals are oriented, and the presence of fractures, all of which affect seismic speeds. The thicknesses and seismic wave speeds are comparable to modern LVZs, suggesting that LVZs mark zones of deformation between tectonic plates. These results can help us better understand how plates move past each other in modern subduction zones.

1 Introduction

Modern subduction zones exhibit a nearly-ubiquitous Low Velocity Zone (LVZ) along the downdip extent of the megathrust that is 3-8 km thick and characterized by low velocities and high reflectivity, conductivity, Poisson's ratio (σ), and the corresponding V_p to V_s ratio (V_p/V_s) (e.g., Audet & Bürgmann, 2014; Audet & Kim, 2016; Bostock, 2013; Y. Kim et al., 2014; Song et al., 2009; Toya et al., 2017) (Fig. 1a-b), all consistent with near-lithostatic pore fluid pressures (P_f) (Audet et al., 2009; Bostock, 2013; Eberhart-Phillips et al., 1989; Hansen et al., 2012; Peacock et al., 2011). Because near-lithostatic P_f affects seismic velocities more than lithologic variations, the rock types that occupy the LVZ - dominantly mafic (Audet & Schaeffer, 2018; Bostock, 2013; Hansen et al., 2012), dominantly sedimentary (Abers et al., 2009; Calvert et al., 2011; Delph et al., 2021), or a combination (Bostock, 2013; Delph et al., 2018) - remain unclear from geophysical data. The LVZ has been interpreted as the overpressurized and relatively undeformed mafic crust sealed beneath a low-permeability fault or narrow interface shear zone (Bostock, 2013; Calvert et al., 2020; Hansen et al., 2012; Kurashimo et al., 2013) (Fig. 1c), or alternatively, as a distributed viscous interface shear zone composed of mixed lithologies, including metasediments (Audet & Schaeffer, 2018; Calvert et al., 2020; Delph et al., 2018, 2021; Nedimović et al., 2003) (Fig 1c).

Distinguishing between these endmember interpretations has important implications for rheological properties of the deep subduction interface and associated seismic and transient deformation patterns. Transient seismic and aseismic slip - e.g., episodic tremor and slow slip, slow slip events, and low frequency earthquakes - are very commonly collocated with LVZs (Audet & Kim, 2016; Calvert et al., 2020; Delph et al., 2018; Hirose et al., 2008;

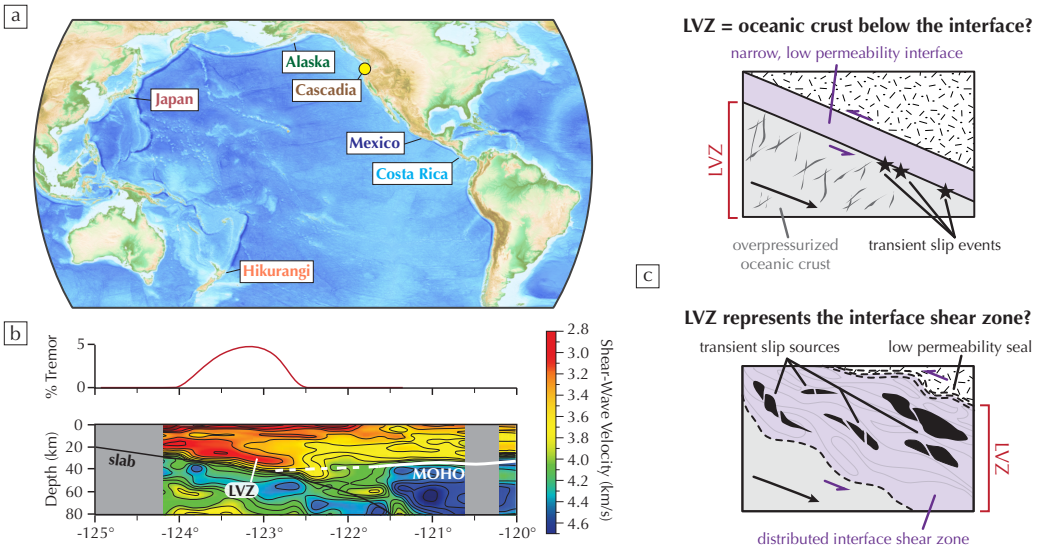

Figure 1. The LVZ (labelled margins in (a); example cross-section at yellow circle of shear wave velocity structure from receiver functions in (b), after Delph et al. (2018)) in modern subduction zones is collocated with transient seismic and aseismic slip (e.g., tremor frequency plot in (b), Delph et al. (2018)). Base map in (a) produced in GPlates (Müller et al., 2018). c) The LVZ is interpreted as the mafic crust below a narrow interface or encompassing a distributed interface shear zone.

Song et al., 2009) (Fig. 1b). Understanding these transient events, which factor into slip budgets and stress regimes related to megathrust earthquake probability (e.g., Rogers & Dragert, 2003; Wech et al., 2009), is crucial for hazard analysis, but both frictional slip along a discrete heterogeneous fault (e.g., Chestler & Creager, 2017; Ito et al., 2007; Lay et al., 2012; Luo & Ampuero, 2018; Shelly et al., 2006) or mixed brittle-viscous deformation within a distributed shear zone (e.g., Beall et al., 2019; Behr et al., 2018; Hayman & Lavier, 2014; Kotowski & Behr, 2019; Tarling et al., 2019; Ujiie et al., 2018) (Fig. 1c) are plausible sources. In addition, the composition and viscosity of the interface control coupling between the overriding and downgoing plates, contributing to, for example, slab velocities (Behr & Becker, 2018), upper plate topography (e.g., Delph et al., 2021), trench behavior (Čížková & Bina, 2013), underplating and recycling of material to the mantle (Bialas et al., 2011; Tewksbury-Christle et al., 2021), and slab morphology (Čížková & Bina, 2013). The LVZ thus provides a possible window into the location and distribution of the subduction interface and the processes along it, which can be used to characterize modern subduction zones.

Investigations into subduction zone LVZs traditionally involve reflection seismology and/or receiver function waveform inversions. Here we take a complementary approach to investigating the LVZ by constraining the seismic signature of a shear zone that once occupied the subduction interface and is now exhumed. We focus on the Condrey Mountain Schist (CMS) in the Klamath Mountains of northern California/southern Oregon: a prograde, greenschist/epidote-amphibolite to epidote-blueschist facies, sediment-dominated subduction complex exhumed from depths where the LVZ is recognized in modern subduction zones (Bostock, 2013; Helper, 1986; Tewksbury-Christle et al., 2021). Previous work established the subduction context of the CMS and provided a structural framework for interpreting pulses of deformation and underplating through time (Helper, 1986; Tewksbury-Christle et al., 2021). We use estimates of shear zone width, occupying rock types, and deformation styles to quantify the CMS' seismic properties during subduction. Our results

suggest that the CMS interface shear zone was seismically anomalous due to mineral and fracture anisotropy, with elevated V_p/V_s consistent with modern LVZs.

2 An exhumed subduction shear zone in the Klamath mountains

The CMS is a Late Jurassic to Early Cretaceous subduction complex on the Oregon-California border that occupies a window through the older, overriding Klamath terranes (Helper, 1986; Snoke & Barnes, 2006) and sits inboard of the younger Franciscan Complex (Dumitru et al., 2010) (Fig. 2a). The CMS comprises two main units with limited retrogression - the upper CMS (greenschist to epidote-amphibolite facies) and the lower CMS (epidote-blueschist facies). The lower CMS is dominantly epidote-blueschist facies schist intercalated with m- to km-scale lenses of mafic epidote blueschist and serpentinized ultramafics; it was subducted to 350-450°C and 0.8-1.1 GPa (∼15°C/km, 30-40 km) (Helper, 1986; Tewksbury-Christle et al., 2021) (Fig. 2b). This geothermal gradient is similar to estimated gradients for warm subduction zones, such as Cascadia, Mexico, Columbia/Equador, and south-central Chile (Syracuse et al., 2010). The lower CMS schist protolith subducted along a sediment-poor margin that was tectonically erosive up dip of final CMS underplating depths (Tewksbury-Christle et al., 2021), similar to the shallow erosion and deep underplating occurring along the modern Hikurangi margin (Bassett et al., 2010; Eberhart-Phillips & Chadwick, 2002).

Neogene doming (Mortimer & Coleman, 1985) exposes 10+ km of lower CMS structural thickness, allowing for detailed characterization of interface shear zone deformation and occupying lithologies. Tewksbury-Christle et al. (2021) identified three progressively underplated subduction interface shear zones (upper, middle, and lower sheets) in the lower CMS, of different thicknesses and formed at different times (Fig. 2b). Here we focus on the middle sheet, for which both the upper and lower shear zone boundaries are preserved, allowing us to constrain shear zone thickness. Tewksbury-Christle et al. (2021) documented two phases of strain localization within the middle sheet. An early stage of distributed deformation occurred over ∼3 km thickness of dominantly schist (94%) with minor mafic blueschist and serpentinite components (Fig. 2c). Following this stage of distributed deformation, introduction of km-scale serpentinite lenses to the subduction interface allowed for temporary strain localization in serpentinite to <10 m thickness proximal to the thrusts along which the lower CMS was assembled (Fig. 2b) (Helper, 1986; Tewksbury-Christle et al., 2021).

Distributed prograde ductile deformation in the CMS middle sheet resulted in a well-developed foliation across the heterogeneous lithologies (Fig. 2b, d-e). In the schist, a closely-spaced cleavage-microlithon fabric defined by alternating bands of quartz and graphite + aligned white mica is pervasively developed, consistent with pressure solution creep as the dominant deformation mechanism (e.g., Bell & Cuff, 1989; Durney, 1972; Passchier & Trouw, 2005). In mafic blueschists, Na-amphiboles are elongated within the foliation plane and define a stretching lineation. In addition to the ductile deformation, cm-scale quartz nodules are common in both the schist and mafic blueschist and have elongated tails parallel to foliation (Fig. 3d-e). We interpret these nodules as prograde dilational fractures/veins that were cyclically emplaced during progressive deformation, and variably transposed by subsequent ductile deformation, as part of the pressure solution process.

3 Methods

We estimated the CMS seismic properties for four different endmember assumptions, including: 1) isotropic (Abers & Hacker, 2016), 2) anisotropic (MATLAB Seismic Anisotropy Toolbox, MSAT) (Walker & Wookey, 2012), 3) fractured isotropic (randomly-oriented fractures, Peacock et al. (2011) and O'Connell & Budiansky (1974); oriented fractures, Hudson (1981) via MSAT; Text S1), and 4) fractured anisotropic (Hudson, 1981; Walker & Wookey, 2012) lithologies. These four scenarios bracket the predicted seismic signature of the CMS

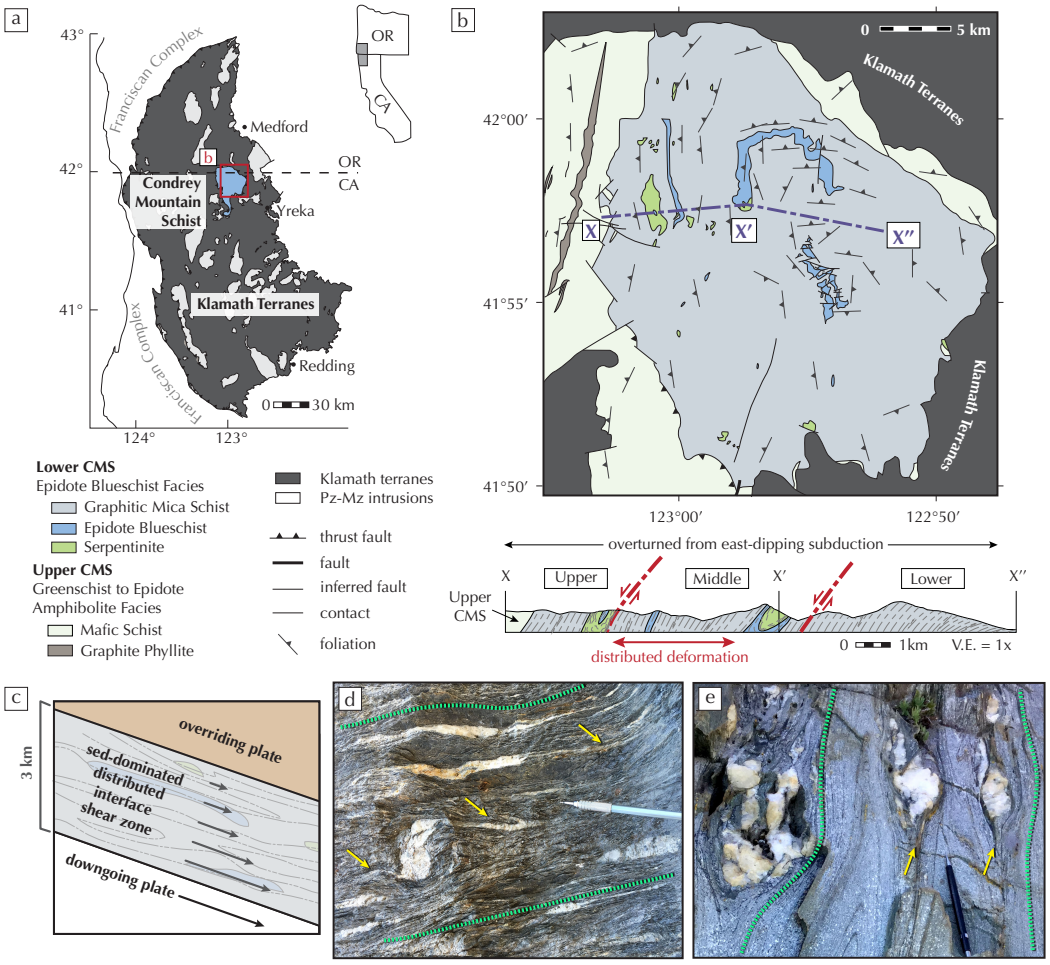

Figure 2. a) Regional setting of the Klamath terranes (dark gray), Franciscan (white), and CMS (blue) (after Snoke & Barnes (2006)). b) Geologic map and cross section of the CMS (after Helper (1986); Tewksbury-Christle et al. (2021)). Distributed deformation occurred between ductile thrust faults (red lines). c) Schematic of the fossil subduction interface shear zone. d-e) Quartz nodules in schist (d) and mafic blueschist (e) with tails (yellow arrows) elongated along foliation planes (teal lines) interpreted as prograde relict veins.

shear zone by characterizing the baseline velocities (1), as well as the independent (2-3) and cumulative effects (4) of mineral and fracture anisotropy.

All synthetic lithologies use CMS mineral and rock volume fractions based on rocks preserved in the middle sheet averaged over thin section- to map-scale (Tables S1-2). MSAT matrix velocities used in anisotropic and fractured anisotropic lithologies are not corrected for pressure-temperature (P-T) conditions because the effects are negligible (<0.05%, Table S3). For cases that included mineral anisotropy, we assumed interface-parallel foliations with crystallographic preferred orientations (CPOs) for aligned minerals (c-axis perpendicular to foliation: white mica; c-axis parallel to lineation: glaucophane) based on observations from mineral fabrics in similar exhumed subduction complexes (Cao & Jung, 2016; Keppler et al., 2017; D. Kim et al., 2013; Kotowski & Behr, 2019) (Fig. S1). For cases that included fracture anisotropy, we averaged porosity, calculated as measured vein area divided by total area, and aspect ratios over thin section, hand sample, and outcrop scales (Table S4). We assume there is no significant 3D anisotropy and that primary fracture orientations were open parallel to lineation and perpendicular to foliation in the schist, consistent with Mohr-Coulomb theory for extensional fracturing (Sibson, 1998) and with similar observations in several other subduction complexes (e.g., Fagereng, 2011; D. Fisher & Byrne, 1987; D. M. Fisher & Brantley, 2014) (Fig. S2). We estimated fracture-fill seismic properties at CMS P-T conditions from water thermodynamic properties (Burnham et al., 1969). For cases with both mineral and fracture anisotropy, we merged MSAT's stiffness tensors derived for the mineral anisotropy and oriented fracture anisotropy cases and calculated velocities from the merged tensor (Text S2). For all MSAT velocities, we averaged the shear wave splitting velocities (V_{s1} and V_{s2}) and calculated V_p/V_s and Poisson's ratio (σ) using V_s^{avg} (Fig. 3-4). Table S5 presents V_{s1} and V_{s2}.

4 Results

V_p/V_s, assuming isotropic lithologies for the 3-km-thick CMS interface shear zone is low (Fig. 4), consistent with experimental measurements of quartz at 1 GPa (Christensen, 1996). Introducing mineral or fracture anisotropy, or a combination, however, results in highly anisotropic V_p/V_s with maximums greater than isotropic values (Fig. 3). Incidence angles that illuminate maximum and minimum V_p/V_s depend on the anisotropy assumptions. Maximum V_p/V_s for anisotropic lithologies is in the foliation plane at low angle to the lineation, and minimum V_p/V_s is at high angles to the lineation (Fig. 3a). In contrast, maximum V_p/V_s for fractured isotropic lithologies with 10% porosity, as constrained from our vein measurements, is in a plane normal to the lineation, and minimum V_p/V_s is at low angles to the lineation (Fig. 3b). Although assumed fracture orientation controls V_p/V_s anisotropy, ratios calculated for randomly oriented fractures at 10% porosity are also higher than for isotropic lithologies (Fig. 4). The effect sums for fractured anisotropic lithologies, with maximum V_p/V_s occurring in the foliation plane but near-perpendicular to the lineation, and minimum V_p/V_s occurring at high angles to the lineation (Fig. 3c).

If we consider teleseismic waves with near-vertical incidence angles (i.e., perpendicular to the foliation), both anisotropic and fractured anisotropic lithologies have a small local V_p/V_s maximum perpendicular to the foliation that is higher than isotropic values (Fig. 3a and c). Fractured isotropic lithologies are maximum for this incidence angle (Fig. 3b).

5 Discussion

The preservation of strong mineral and fracture anisotropy in the CMS shear zone leads us to interpret our fractured anisotropic lithology results as the best-constrained prediction of shear zone seismic velocities during prograde deformation. Estimated V_p/V_s for the fractured anisotropic case and foliation-perpendicular arrivals is anomalously high (ca. 2.0, $\sigma = 0.33$, Fig. 4a). Modern subduction zones have LVZs with slow V_p and V_s (up to 70% slower for V_s, see Fig. S3 for comparison of estimated CMS V_s and modern LVZs), and

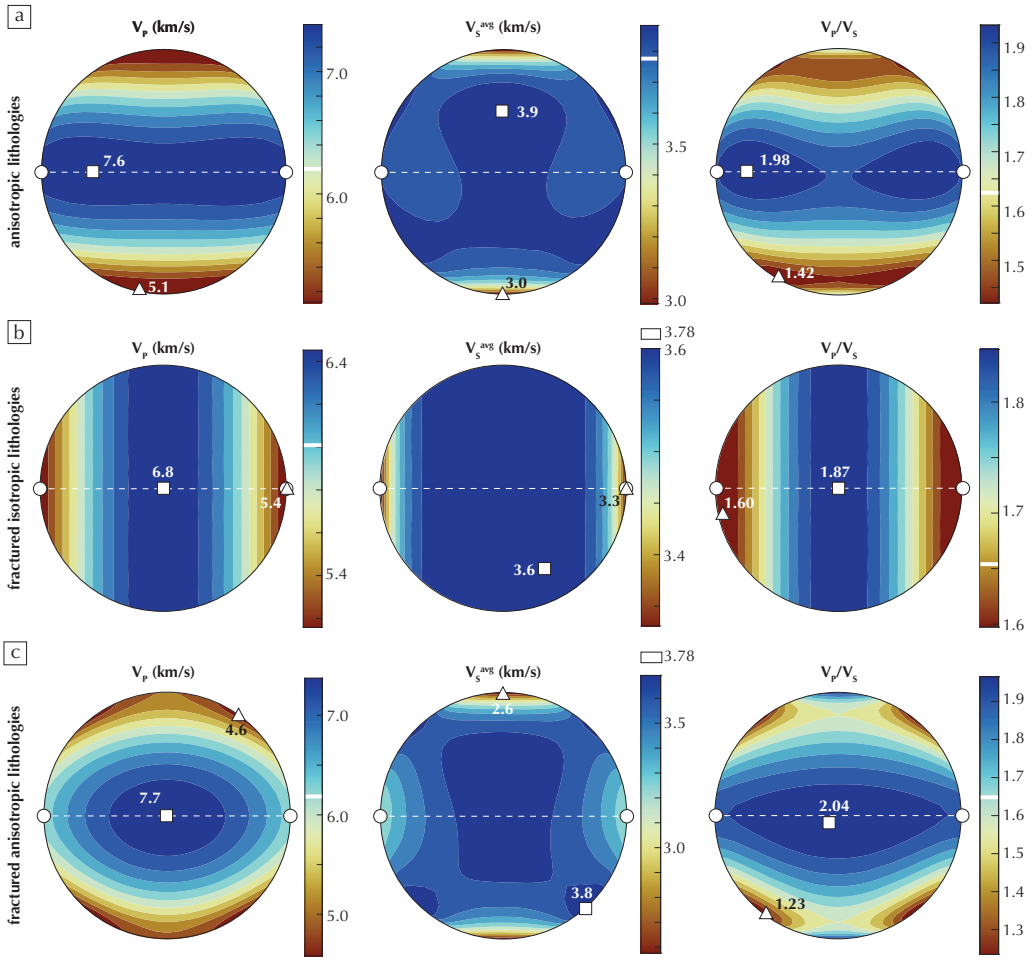

Figure 3. Pole figures showing the calculated CMS seismic signature accounting for mineral anisotropy (a), fracture anisotropy (b), and both (c). Squares and triangles mark the maximum and minimum values, respectively. Assumed foliation (white dashed line) and lineation (white circles) are given for orientation, and white bars mark the isotropic values.

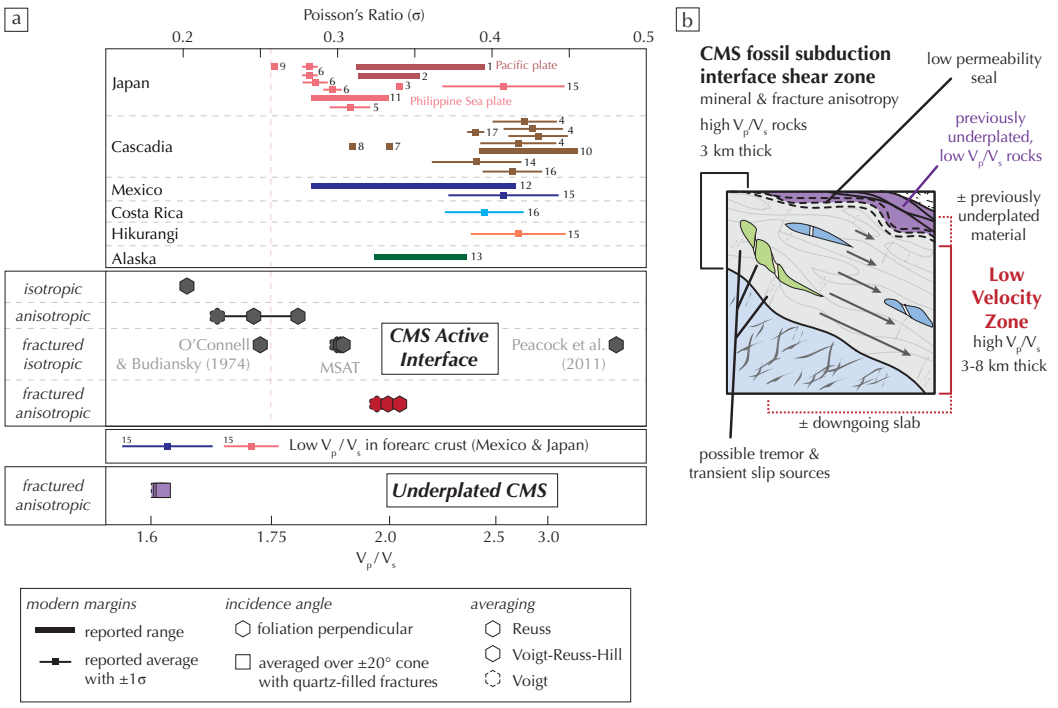

Figure 4. a) Comparison of seismic signatures from modern subduction zones (Toya et al. (2017)[1], Tsuji et al. (2008)[2], Kodaira et al. (2004)[3], Hansen et al. (2012)[4], Kato et al. (2010)[5], Matsubara et al. (2009)[6], Delph et al. (2018)[7], Calkins et al. (2011)[8], Fukao et al. (1983)[9], Audet & Schaeffer (2018)[10], Kato et al. (2014)[11], Y. Kim et al. (2010)[12], Y. Kim et al. (2014)[13], Audet et al. (2009)[14], Audet & Bürgmann (2014)[15], Audet & Schwartz (2013)[16], Peacock et al. (2011)[17]) and calculated from the CMS (hexagons and squares). Hexagons are for incidence angles perpendicular to the foliation, with the red hexagon indicating CMS seismic properties during prograde deformation. Outlines differentiate between averaging schemes used to derive bulk stiffness tensors. The purple squares are averaged over a ±20° cone in azimuth and elevation centered on the foliation-perpendicular axis, include mineralized quartz fractures, and indicate CMS seismic properties after underplating. b) Schematic showing the CMS subduction interface shear zone as part of the LVZ, with possible contributions from the downgoing slab and previously underplated material, and the relationship to transient seismic and aseismic slip source regions.

high V_p/V_s (1.8-3.3, $\sigma = 0.28 - 0.45$) (Figs. 1a-b and 4a) (e.g., Audet & Bürgmann, 2014; Audet & Kim, 2016; Bostock, 2013; Y. Kim et al., 2014; Song et al., 2009; Toya et al., 2017). Our results incorporating anisotropy and fracture porosity demonstrate that even quartz-rich metasedimentary rocks can reach the lower bounds of the high V_p/V_s values in modern subduction zones (Fig. 4a). The very high V_p/V_s values (e.g. > 2.0, $\sigma > 0.33$) cannot be reproduced in our analysis, however. This may imply higher porosity in these regions or overestimated V_p/V_s and underestimated thicknesses due to the tradeoff between calculated thickness and V_p/V_s in receiver function studies (e.g., Bostock, 2013).

Because the V_p/V_s range for modern LVZs is higher on average than values for isotropic rocks at LVZ depths (<2.0) (Christensen, 1996), LVZs are typically attributed to high P_f (Audet et al., 2009; Bostock, 2013; Hansen et al., 2012; Peacock et al., 2011) based on experimental work correlating high V_p/V_s and high P_f (Christensen, 1996; Eberhart-Phillips et al., 1989), where high P_f maintains significant porosity at high confining pressures (e.g., Eberhart-Phillips et al., 1989). This is consistent with our observations in the CMS shear zone of abundant quartz veins that were emplaced during brittle fracture associated with pressure solution creep. Empirical relationships and magnetotelluric studies suggest 0.5-4% porosity is needed to match LVZ velocities (Calvert et al., 2020; Peacock et al., 2011). Our estimates of up to 10% porosity are higher, but our calculated V_p/V_s is still compatible with V_p/V_s in modern environments because we also take into account mineral anisotropy. Porosities of up to 10% are compatible with vein exposure measurements in other subduction complexes exhumed from similar conditions, (e.g., 4-11%, Muñoz-Montecinos et al. (2020)), so these slightly higher values may be more representative than existing experimental constraints.

Observations from the CMS fossil shear zone are also consistent with estimated LVZ thicknesses and some interpretations of the rock types that define the LVZ. Thickness estimates from modern LVZs range from ~3-8 km (Abers et al., 2009; Audet et al., 2009; Audet & Kim, 2016; Audet & Schaeffer, 2018; Audet & Schwartz, 2013; Bostock, 2013; Delph et al., 2018; Hansen et al., 2012; Hirose et al., 2008; Y. Kim et al., 2014, 2010; Nedimović et al., 2003; Song et al., 2009; Toya et al., 2017) with along-strike and down-dip thickness variations (Audet & Schaeffer, 2018; Delph et al., 2018; D. Kim et al., 2019; Toya et al., 2017). The width of the CMS middle sheet was distributed over ~3 km, comparable with the lower end of these LVZ thicknesses. Furthermore, the shear zone was dominated by metasedimentary protoliths, consistent with interpretations that the LVZ represents deforming and underplating sedimentary packages (e.g., Abers et al., 2009; Calvert et al., 2011; Delph et al., 2021), as opposed to overpressurized and relatively undeformed mafic crust. Sediment prevalence at depth in the CMS interface shear zone, despite subducting along a sediment-poor, tectonically erosive margin, required stacking of thin incoming sediment packages through protracted underplating and entrainment (Tewksbury-Christle et al., 2021). Down-dip thickening observed in modern LVZs (Abers et al., 2009; Hansen et al., 2012; Toya et al., 2017) may be indicative of this progressive underplating process and may be independent of incoming sediment supply, contrary to previous assumptions (Hansen et al., 2012). Thicker LVZs may be explained by thicker incoming sediment packages or alternatively through additional contributions from previously underplated material and/or the overpressurized downgoing slab (Fig. 4b).

The fluid-filled fracture anisotropy that we include in the CMS best estimate of seismic properties represents the subduction interface while it was *actively* deforming. However, once subducted material is detached from the downgoing slab and accreted to the upper plate via underplating, mineralization of fractures would change the fracture fill properties. To examine the potential seismic properties for this scenario, we used quartz properties for the fracture fill and averaged values over a ±20° cone in azimuth and elevation centered on foliation-perpendicular incidence angles to account for variations in kinematics during protracted underplating (squares, Fig. 4a). The resulting V_s (3.18 km/s) and 20°-averaged V_p/V_s are anomalously low. Audet & Bürgmann (2014) previously interpreted low V_p/V_s at

the base of the forearc crust in Japan and Mexico (Fig. 4a) as silica enrichment. Delph et al. (2018, 2021) interpreted low V_s (<3.2 km/s) at the base of the forearc crust in Cascadia as hydrated underplated metasediments. Our results are consistent with these interpretations, e.g. that these zones may represent previously underplated and abandoned metasedimentary material in the upper plate hanging wall or forearc region with mineralized quartz veins.

It is important to note that these predicted velocities are highly dependent on our assumptions. Our reported porosity is a maximum as it assumes that all fractures are open simultaneously. Combining maximum porosity and 'perfect' CPOs for aligned minerals results in the largest deviation possible from isotropic values based on our rock record constraints. Decreasing porosity and/or varying mineral alignment will approach isotropic values. Furthermore, velocity behavior with incidence angle is strongly controlled by assumed fracture orientation (Fig. 3). Foliation-parallel veins observed in the Makimine mélange suggest that extreme fluid overpressure can transiently rotate σ_1 by 90° (Ujiie et al., 2018). In the case of our assumptions, this rotates the velocity anisotropy 90° such that V_p/V_s is anomalously low perpendicular to the foliation. Although vertical σ_1 is most common for underplated sediments in subduction zones based on rock record analyses (e.g., D. Fisher & Byrne, 1987), variations in the stress state could affect observed velocity patterns. Validity of these assumptions could therefore be tested by examining LVZ signatures with respect to incidence angle, which could help to deconvolve mineral and fracture anisotropy contributions, lithologic variations, and fracture orientations.

Our interpretation that LVZs in subduction zones may be consistent with a wide, sediment-dominated shear zone deforming at high P_f also has implications for the source region and processes involved in slow slip and tremor. Transient seismic (e.g., low frequency earthquakes, LFEs) and aseismic slip (e.g., slow slip events) occur collocated with LVZs in modern subduction zones (e.g., Audet & Kim, 2016; Calvert et al., 2020; Delph et al., 2018; Hirose et al., 2008; Song et al., 2009). Temporal and spatial correlation of LFEs, tremor, and slow slip events suggest a genetic connection (Beroza & Ide, 2009; Obara & Hirose, 2006). Competing models for event sources invoke: 1) frictional slip on a heterogeneous fault (e.g., Chestler & Creager, 2017; Ito et al., 2007; Lay et al., 2012; Luo & Ampuero, 2018; Shelly et al., 2006) or 2) frictional failure of blocks or frictionally-weak slip planes within a distributed ductile shear zone (e.g., Beall et al., 2019; Behr et al., 2018; Chestler & Creager, 2017; Hayman & Lavier, 2014; Kotowski & Behr, 2019; Tarling et al., 2019; Ujiie et al., 2018). Distinguishing between these two endmember models has important implications for estimating LFE and slow slip source properties, such as slip amount, stress drop and recurrence (Behr & Bürgmann, 2021; Chestler & Creager, 2017; Frank et al., 2018). The observations that the CMS shear zone 1) accommodated subduction-related deformation over a 3-km-thick zone, 2) records seismic properties that are compatible with modern LVZs, and 3) shows evidence for transient frictional vein emplacement during broader viscous deformation, all lend support to the latter model of distributed frictional-viscous deformation dominating the deep subduction interface in the slow slip and tremor source region (Fig. 4b).

6 Conclusions

We used estimates of deformation zone thickness, fabric anisotropy, and fracture porosity from a fossil subduction interface shear zone, now exposed at the surface, to calculate its seismic properties for comparison to LVZs in modern subduction zones. This fossilized subduction shear zone exhibits several features in common with modern LVZs, including a) distributed deformation over a 3 km thick shear zone, compatible with observed LVZ thicknesses, b) rock types that are consistent with low V_p and V_s velocities, and c) mineral and fracture anisotropy that result in anomalously high V_p/V_s for near-vertical incidence angles. These observations suggest that LVZs in modern subduction zones are compatible with a sediment-dominated, distributed, subduction interface shear zone deforming under elevated fluid pressures, rather than overpressurized, undeformed oceanic crust located be-

low the interface. This interpretation implies that zones of slow slip and tremor, commonly collocated with LVZs, record deformation within distributed frictional-viscous shear zones rather than along discrete fault planes.

Acknowledgments

All data collected by the authors will be available and have an associated DOI from the ETH Research Collection data repository. For review purposes, data are included in the Supporting Information document.

This work was supported by a National Science Foundation (NSF) CAREER Grant (EAR-1555346) and a European Research Council (ERC) Starting Grant (947659) awarded to W.M. Behr. We are grateful to Dr. Mark Helper for help with field data collection and analysis of the tectonic history, Dr. Thorsten Becker for insightful feedback that helped strengthen this manuscript, and the Rogue River-Siskyou National Forest for supporting our fieldwork.

References

Abers, G. A., & Hacker, B. R. (2016). A MATLAB toolbox and Excel workbook for calculating the densities, seismic wave speeds, and major element composition of minerals and rocks at pressure and temperature. *Geochemistry, Geophysics, Geosystems*, *17*(2), 616–624.

Abers, G. A., MacKenzie, L. S., Rondenay, S., Zhang, Z., Wech, A. G., & Creager, K. C. (2009). Imaging the source region of Cascadia tremor and intermediate-depth earthquakes. *Geology*, *37*(12), 1119–1122.

Audet, P., Bostock, M. G., Christensen, N. I., & Peacock, S. M. (2009). Seismic evidence for overpressured subducted oceanic crust and megathrust fault sealing. *Nature*, *457*(7225), 76–78.

Audet, P., & Bürgmann, R. (2014). Possible control of subduction zone slow-earthquake periodicity by silica enrichment. *Nature*, *510*(7505), 389–392.

Audet, P., & Kim, Y. (2016). Teleseismic constraints on the geological environment of deep episodic tremor and slow earthquakes in subduction zone forearcs: a review. *Tectonophysics*, *670*, 1–15.

Audet, P., & Schaeffer, A. J. (2018). Fluid pressure and shear zone development over the locked to slow slip region in Cascadia. *Science advances*, *4*(3).

Audet, P., & Schwartz, S. Y. (2013). Hydrologic control of forearc strength and seismicity in the Costa Rican subduction zone. *Nature Geoscience*, *6*(10), 852–855.

Bassett, D., Sutherland, R., Henrys, S., Stern, T., Scherwath, M., Benson, A., ... Henderson, M. (2010). Three-dimensional velocity structure of the northern Hikurangi margin, Raukumara, New Zealand: Implications for the growth of continental crust by subduction erosion and tectonic underplating. *Geochemistry, Geophysics, Geosystems*, *11*(10), 1–24.

Beall, A., Fagereng, Å., & Ellis, S. (2019). Strength of strained two-phase mixtures: Application to rapid creep and stress amplification in subduction zone mélange. *Geophysical Research Letters*, *46*(1), 169–178.

Behr, W. M., & Becker, T. W. (2018). Sediment control on subduction plate speeds. *Earth and Planetary Science Letters*, *502*, 166–173.

Behr, W. M., & Bürgmann, R. (2021). What's down there? the structures, materials and environment of deep-seated slow slip and tremor. *Philosophical Transactions of the Royal Society A*, *379*(2193).

Behr, W. M., Kotowski, A. J., & Ashley, K. T. (2018). Dehydration-induced rheological heterogeneity and the deep tremor source in warm subduction zones. *Geology*, *46*(5), 475–478.

Bell, T., & Cuff, C. (1989). Dissolution, solution transfer, diffusion versus fluid flow and volume loss during deformation/metamorphism. *Journal of Metamorphic Geology*, *7*(4),

425–447.

Beroza, G. C., & Ide, S. (2009). Deep tremors and slow quakes. *Science*, *324*(5930), 1025–1026.

Bialas, R. W., Funiciello, F., & Faccenna, C. (2011). Subduction and exhumation of continental crust: Insights from laboratory models. *Geophysical Journal International*, *184*(1), 43–64.

Bostock, M. (2013). The Moho in subduction zones. *Tectonophysics*, *609*, 547–557.

Burnham, C. W., Holloway, J. R., & Davis, N. F. (1969). *Thermodynamic Properties of Water to 1,000° C and 10,000 Bars*. Geological Society of America.

Calkins, J. A., Abers, G. A., Ekström, G., Creager, K. C., & Rondenay, S. (2011). Shallow structure of the Cascadia subduction zone beneath western Washington from spectral ambient noise correlation. *Journal of Geophysical Research: Solid Earth*, *116*(B7).

Calvert, A. J., Bostock, M. G., Savard, G., & Unsworth, M. J. (2020). Cascadia low frequency earthquakes at the base of an overpressured subduction shear zone. *Nature communications*, *11*(1), 1–10.

Calvert, A. J., Preston, L. A., & Farahbod, A. M. (2011). Sedimentary underplating at the Cascadia mantle-wedge corner revealed by seismic imaging. *Nature Geoscience*, *4*(8), 545–548.

Cao, Y., & Jung, H. (2016). Seismic properties of subducting oceanic crust: Constraints from natural lawsonite-bearing blueschist and eclogite in Sivrihisar Massif, Turkey. *Physics of the Earth and Planetary Interiors*, *250*, 12–30.

Chestler, S., & Creager, K. (2017). Evidence for a scale-limited low-frequency earthquake source process. *Journal of Geophysical Research: Solid Earth*, *122*(4), 3099–3114.

Christensen, N. I. (1996). Poisson's ratio and crustal seismology. *Journal of Geophysical Research: Solid Earth*, *101*(B2), 3139–3156.

Čížková, H., & Bina, C. R. (2013). Effects of mantle and subduction-interface rheologies on slab stagnation and trench rollback. *Earth and Planetary Science Letters*, *379*, 95–103.

Delph, J. R., Levander, A., & Niu, F. (2018). Fluid controls on the heterogeneous seismic characteristics of the Cascadia margin. *Geophysical Research Letters*, *45*(20), 11–021.

Delph, J. R., Thomas, A. M., & Levander, A. (2021). Subcretionary tectonics: Linking variability in the expression of subduction along the Cascadia forearc. *Earth and Planetary Science Letters*, *556*, 116724.

Dumitru, T. A., Wakabayashi, J., Wright, J. E., & Wooden, J. L. (2010). Early Cretaceous transition from nonaccretionary behavior to strongly accretionary behavior within the Franciscan subduction complex. *Tectonics*, *29*, 1–24.

Durney, D. (1972). Solution-transfer, an important geological deformation mechanism. *Nature*, *235*(5337), 315–317.

Eberhart-Phillips, D., & Chadwick, M. (2002). Three-dimensional attenuation model of the shallow Hikurangi subduction zone in the Raukumara Peninsula, New Zealand. *Journal of Geophysical Research: Solid Earth*, *107*(B2), ESE–3.

Eberhart-Phillips, D., Han, D.-H., & Zoback, M. (1989). Empirical relationships among seismic velocity, effective pressure, porosity, and clay content in sandstone. *Geophysics*, *54*(1), 82–89.

Fagereng, Å. (2011). Fractal vein distributions within a fault-fracture mesh in an exhumed accretionary mélange, Chrystalls Beach Complex, New Zealand. *Journal of Structural Geology*, *33*(5), 918–927.

Fisher, D., & Byrne, T. (1987). Structural evolution of underthrusted sediments, Kodiak Islands, Alaska. *Tectonics*, *6*(6), 775–793.

Fisher, D. M., & Brantley, S. L. (2014). The role of silica redistribution in the evolution of slip instabilities along subduction interfaces: Constraints from the Kodiak accretionary complex, Alaska. *Journal of Structural Geology*, *69*, 395–414.

Frank, W. B., Rousset, B., Lasserre, C., & Campillo, M. (2018). Revealing the cluster of slow transients behind a large slow slip event. *Science advances*, *4*(5).

Fukao, Y., Hori, S., & Ukawa, M. (1983). A seismological constraint on the depth of

basalt–eclogite transition in a subducting oceanic crust. *Nature*, *303*(5916), 413–415.

Hansen, R. T., Bostock, M. G., & Christensen, N. I. (2012). Nature of the low velocity zone in Cascadia from receiver function waveform inversion. *Earth and Planetary Science Letters*, *337*, 25–38.

Hayman, N. W., & Lavier, L. L. (2014). The geologic record of deep episodic tremor and slip. *Geology*, *42*(3), 195–198.

Helper, M. (1986). Deformation and high P/T metamorphism in the central part of the Condrey Mountain window, north-central Klamath Mountains, California and Oregon. *GSA Memoir 164*, 125–142.

Hirose, F., Nakajima, J., & Hasegawa, A. (2008). Three-dimensional seismic velocity structure and configuration of the Philippine Sea slab in southwestern Japan estimated by double-difference tomography. *Journal of Geophysical Research: Solid Earth*, *113*(B9).

Hudson, J. A. (1981). Wave speeds and attenuation of elastic waves in material containing cracks. *Geophysical Journal International*, *64*(1), 133–150.

Ito, Y., Obara, K., Shiomi, K., Sekine, S., & Hirose, H. (2007). Slow earthquakes coincident with episodic tremors and slow slip events. *Science*, *315*(5811), 503–506.

Kato, A., Iidaka, T., Ikuta, R., Yoshida, Y., Katsumata, K., Iwasaki, T., ... Hirata, N. (2010). Variations of fluid pressure within the subducting oceanic crust and slow earthquakes. *Geophysical Research Letters*, *37*(14).

Kato, A., Saiga, A., Takeda, T., Iwasaki, T., & Matsuzawa, T. (2014). Non-volcanic seismic swarm and fluid transportation driven by subduction of the Philippine Sea slab beneath the Kii Peninsula, Japan. *Earth, Planets and Space*, *66*(1), 1–8.

Keppler, R., Behrmann, J. H., & Stipp, M. (2017). Textures of eclogites and blueschists from Syros island, Greece: Inferences for elastic anisotropy of subducted oceanic crust. *Journal of Geophysical Research: Solid Earth*, *122*(7), 5306–5324.

Kim, D., Katayama, I., Michibayashi, K., & Tsujimori, T. (2013). Rheological contrast between glaucophane and lawsonite in naturally deformed blueschist from Diablo Range, California. *Island Arc*, *22*(1), 63–73.

Kim, D., Keranen, K. M., Abers, G. A., & Brown, L. D. (2019). Enhanced resolution of the subducting plate interface in central Alaska from autocorrelation of local earthquake coda. *Journal of Geophysical Research: Solid Earth*, *124*(2), 1583–1600.

Kim, Y., Abers, G. A., Li, J., Christensen, D., Calkins, J., & Rondenay, S. (2014). Alaska Megathrust 2: Imaging the megathrust zone and Yakutat/Pacific plate interface in the Alaska subduction zone. *Journal of Geophysical Research: Solid Earth*, *119*(3), 1924–1941.

Kim, Y., Clayton, R., & Jackson, J. (2010). Geometry and seismic properties of the subducting Cocos plate in central Mexico. *Journal of Geophysical Research: Solid Earth*, *115*(B6).

Kodaira, S., Iidaka, T., Kato, A., Park, J.-O., Iwasaki, T., & Kaneda, Y. (2004). High pore fluid pressure may cause silent slip in the Nankai Trough. *Science*, *304*(5675), 1295–1298.

Kotowski, A. J., & Behr, W. M. (2019). Length scales and types of heterogeneities along the deep subduction interface: Insights from exhumed rocks on Syros Island, Greece. *Geosphere*, *15*(4), 1038–1065.

Kurashimo, E., Iwasaki, T., Iidaka, T., Kato, A., Yamazaki, F., Miyashita, K., ... others (2013). Along-strike structural changes controlled by dehydration-related fluids within the Philippine Sea plate around the segment boundary of a megathrust earthquake beneath the Kii peninsula, southwest Japan. *Geophysical research letters*, *40*(18), 4839–4844.

Lay, T., Kanamori, H., Ammon, C. J., Koper, K. D., Hutko, A. R., Ye, L., ... Rushing, T. M. (2012). Depth-varying rupture properties of subduction zone megathrust faults. *Journal of Geophysical Research: Solid Earth*, *117*(B4).

Luo, Y., & Ampuero, J.-P. (2018). Stability of faults with heterogeneous friction properties and effective normal stress. *Tectonophysics*, *733*, 257–272.

Matsubara, M., Obara, K., & Kasahara, K. (2009). High-V_p/V_s zone accompanying non-volcanic tremors and slow-slip events beneath southwestern Japan. *Tectonophysics*, *472*(1-

4), 6–17.

Mortimer, N., & Coleman, R. G. (1985). A Neogene structural dome in the Klamath Mountains, California and Oregon. *Geology*, *13*, 253–256.

Müller, R. D., Cannon, J., Qin, X., Watson, R. J., Gurnis, M., Williams, S., ... Zahirovic, S. (2018). GPlates: building a virtual Earth through deep time. *Geochemistry, Geophysics, Geosystems*, *19*(7), 2243–2261.

Muñoz-Montecinos, J., Angiboust, S., Cambeses, A., & García-Casco, A. (2020). Multiple veining in a paleo–accretionary wedge: The metamorphic rock record of prograde dehydration and transient high pore-fluid pressures along the subduction interface (Western Series, central Chile). *Geosphere*, *16*(3), 765–786.

Nedimović, M. R., Hyndman, R. D., Ramachandran, K., & Spence, G. D. (2003). Reflection signature of seismic and aseismic slip on the northern Cascadia subduction interface. *Nature*, *424*(6947), 416–420.

Obara, K., & Hirose, H. (2006). Non-volcanic deep low-frequency tremors accompanying slow slips in the southwest Japan subduction zone. *Tectonophysics*, *417*(1-2), 33–51.

O'Connell, R. J., & Budiansky, B. (1974). Seismic velocities in dry and saturated cracked solids. *Journal of Geophysical Research*, *79*(35), 5412–5426.

Passchier, C. W., & Trouw, R. A. (2005). *Microtectonics*. Springer Science & Business Media.

Peacock, S. M., Christensen, N. I., Bostock, M. G., & Audet, P. (2011). High pore pressures and porosity at 35 km depth in the Cascadia subduction zone. *Geology*, *39*(5), 471–474.

Rogers, G., & Dragert, H. (2003). Episodic tremor and slip on the Cascadia subduction zone: The chatter of silent slip. *Science*, *300*(5627), 1942–1943.

Shelly, D. R., Beroza, G. C., Ide, S., & Nakamula, S. (2006). Low-frequency earthquakes in Shikoku, Japan, and their relationship to episodic tremor and slip. *Nature*, *442*(7099), 188–191.

Sibson, R. H. (1998). Brittle failure mode plots for compressional and extensional tectonic regimes. *Journal of Structural Geology*, *20*(5), 655–660.

Snoke, A. W., & Barnes, C. G. (2006). The development of tectonic concepts for the Klamath Mountains province, California and Oregon. *Geological Society of America Special Papers 410*, 1–29.

Song, T.-R. A., Helmberger, D. V., Brudzinski, M. R., Clayton, R. W., Davis, P., Pérez-Campos, X., & Singh, S. K. (2009). Subducting slab ultra-slow velocity layer coincident with silent earthquakes in southern Mexico. *Science*, *324*(5926), 502–506.

Syracuse, E. M., van Keken, P. E., & Abers, G. A. (2010). The global range of subduction zone thermal models. *Physics of the Earth and Planetary Interiors*, *183*(1-2), 73–90.

Tarling, M. S., Smith, S. A., & Scott, J. M. (2019). Fluid overpressure from chemical reactions in serpentinite within the source region of deep episodic tremor. *Nature Geoscience*, 1–9.

Tewksbury-Christle, C., Behr, W., & Helper, M. (2021). Tracking deep sediment underplating in a fossil subduction margin: implications for interface rheology and mass and volatile recycling. *Geochemistry, Geophysics, Geosystems*, *22*.

Toya, M., Kato, A., Maeda, T., Obara, K., Takeda, T., & Yamaoka, K. (2017). Down-dip variations in a subducting low-velocity zone linked to episodic tremor and slip: a new constraint from ScSp waves. *Scientific reports*, *7*(1), 1–10.

Tsuji, Y., Nakajima, J., & Hasegawa, A. (2008). Tomographic evidence for hydrated oceanic crust of the Pacific slab beneath northeastern Japan: Implications for water transportation in subduction zones. *Geophysical Research Letters*, *35*(14).

Ujiie, K., Saishu, H., Fagereng, Å., Nishiyama, N., Otsubo, M., Masuyama, H., & Kagi, H. (2018). An explanation of episodic tremor and slow slip constrained by crack-seal veins and viscous shear in subduction mélange. *Geophysical Research Letters*, *45*(11), 5371–5379.

Walker, A. M., & Wookey, J. (2012). MSAT—A new toolkit for the analysis of elastic and seismic anisotropy. *Computers & Geosciences*, *49*, 81–90.

507 Wech, A. G., Creager, K. C., & Melbourne, T. I. (2009). Seismic and geodetic constraints
508 on Cascadia slow slip. *Journal of Geophysical Research: Solid Earth*, *114*(B10).